Seismic properties of the Nazca oceanic crust in southern Peruvian subduction system

YoungHee Kim [a,*], Robert W. Clayton [b]

[a] *School of Earth and Environment Sciences, Seoul National University, Republic of Korea*
[b] *Seismological Laboratory, California Institute of Technology, United States*

A B S T R A C T

The horizontal Nazca slab, extending over a distance of ~800 km along the trench is one of enigmatic features in Peruvian subduction zone. Increased buoyancy of the oceanic lithosphere alone due to the subduction of Nazca Ridge is insufficient to fully explain such a lengthy segment. We use data from the recent seismic experiment in southern Peru to find that the subduction-related hydration plays a major role in controlling shear wave velocities within the upper part of the oceanic crust and overlying materials. We observe substantial velocity reductions of ~20–40% near the top plate interface along- and perpendicular-to the trench from ~40–120 km depths. In particular, significant shear wave velocity reductions and subsequently higher P-to-S velocity ratio (exceeding 2.0) at the flat slab region suggest that the seismically probed layer is fluid-rich and mechanically weak. The dominant source of fluid comes from metasediments and subducted crust (Nazca Ridge). Long-term supply of fluid from the southward migrating Nazca Ridge provides additional buoyancy of the subducting oceanic lithosphere and also lowers the viscosity of the overlying mantle wedge to drive and sustain the flat plate segment of ~800 km along the trench. Also, by comparing calculated seismic velocities with experimentally derived mineral physics data, we additionally provide mechanical constraints on the possible changes in frictional behavior across the subduction zone plate interface. Observed low seismic velocities in the seismogenic zone suggest a presence of low strength materials that may be explained by overpressured pore fluids (i.e., accreted sediment included in the subduction channel).

© 2015 Elsevier B.V. All rights reserved.

1. Introduction

The effects of the aseismic ridge subduction on the subduction dynamics have been long debated. Slab-flattening process have been commonly attributed to the excess buoyancy provided by the subduction of an anomalously thick crust of young oceanic lithosphere, as seismically imaged for Alaska (Kim et al., 2014), or of aseismic ridges, as proposed for South America (Gutscher et al., 2000). Skinner and Clayton (2013) systematically evaluated proposed hypotheses for flat subduction in South America based on the spatial and temporal evidence, and found no simple or obvious explanation for such feature.

Along the South American margin, the Nazca Plate subducts beneath the South American Plate, causing upper-plate deformation, earthquakes, and volcanism (e.g. Cahill and Isacks, 1992; Bilek, 2010). Earthquakes in this region exhibit heterogeneous rup-

ture characteristics, which are related to the subducting asperity on the Nazca Plate (Bilek, 2010). In particular, significant subduction zone complexity in southern Peru (from 14°S to 20°S) has been previously attributed to the moderate-size (approximately 200 km × 18 km) Nazca Ridge and the Nazca fracture zone. This region involves the transition in slab geometry from flat to normal from north to south (Cahill and Isacks, 1992; Hayes et al., 2012; Phillips et al., 2012; Phillips and Clayton, 2014), decrease of magmatic activity towards the flat slab subduction (Ramos and Folguera, 2009), and variability of earthquake rupture pattern and coupling state (Chlieh et al., 2011).

In this paper, we focus on the region of flat-slab subduction, where the Nazca Ridge subducts, normal-dip subduction zone, south of Nazca Ridge, and the region between the two (Figs. 1 and 2), to examine both perpendicular and along-strike variations in the plate interface properties. We use teleseismic earthquakes recorded from the Peru Subduction Experiment (PeruSE), and then relate obtained seismic properties, such as slab geometry and seismic velocities, to infer the subducted materials near the plate interface and the degree of hydration, and to understand present-day subduction dynamics beneath southern Peru.

* Corresponding author.
E-mail addresses: younghkim@snu.ac.kr (Y. Kim), clay@gps.caltech.edu (R.W. Clayton).
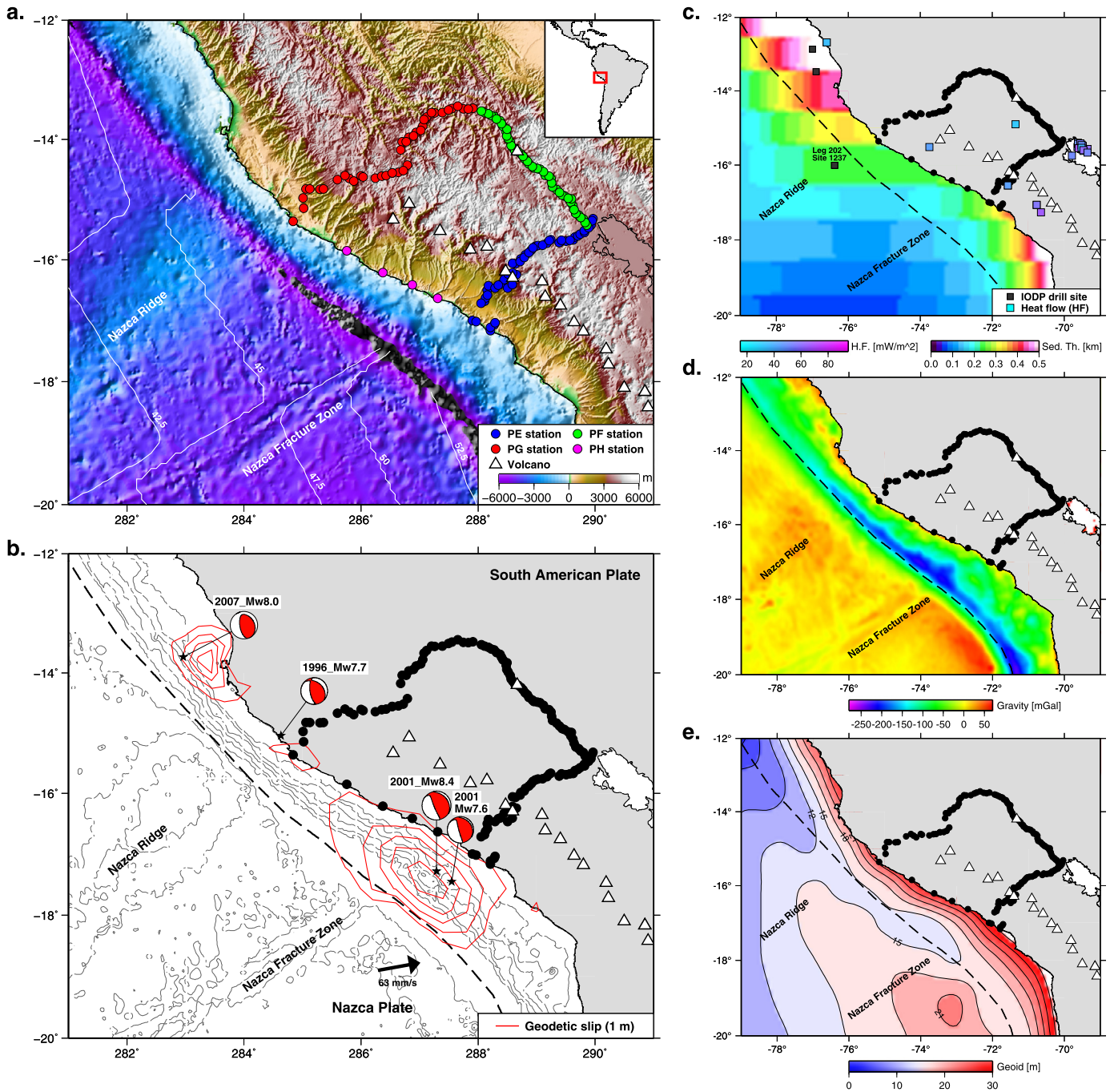
Fig. 1. Geophysical datasets probing the subducted Nazca Plate beneath southern Peru. Locations of broadband seismic stations, volcanoes, and bathymetric anomalies (Nazca Ridge and Nazca fracture zone) are shown as circles, triangles, and texts in all panels (a–e). a. Topographic–bathymetric map showing the region of the study. Each seismic profile of Peru Subduction Experiment is shown as a different colored circle. The age of incoming Nazca Plate is shown as a white text. b. Seismotectonic setting of southern Peru with rupture of large-magnitude ($Mw > 7.5$) earthquakes on the Peru megathrust. Red contours represent slip distributions of the 2007 $Mw = 7.0$ Pisco, 1996 $Mw = 7.7$ Nazca, and 2001 $Mw = 7.6$ & 8.4 Arequipa earthquakes, and they were determined from joint inversions of the InSAR and GPS data (Chlieh et al., 2011). The source mechanisms of the earthquakes are from the global CMT catalog (Ekström et al., 2012). c. Sediment thickness (Laske and Masters, 1997), and heat flow data (colored squares; Pollack et al., 1993). IODP drill hole sites are shown as gray squares. d. Gravity anomaly (Sandwell et al., 2013). e. Geoid (Förste et al., 2008). (For interpretation of the colors in this figure, the reader is referred to the web version of this article.)

2. Bathymetric anomalies on the subducting Nazca plate

Although the correlation between the subduction of the bathymetric anomaly and the change in the subduction angle in southern Peru is not yet clear, its influence on the plate interface properties appears apparent. The variability of subducted materials (thickness of the trench sediment) and/or the roughness of the seafloor strongly influence the interplate coupling and transient slip along the subduction interface (Perfettini et al., 2010;

Chlieh et al., 2011; Wang and Bilek, 2014). Furthermore, the processes of sediment compaction and dehydration, and/or other reactions within the fault zone materials can bring about changes in strength or fluid pressure along the plate boundary thrust zone. Scattered coda of teleseismic P waves, such as in receiver functions, often show a thin low-velocity layer corresponding to the top of the subducting plate. These have been best documented in Mexico (Kim et al., 2010, 2012a, 2013), Alaska (Kim et al., 2014), and Cascadia (Hansen et al., 2012), where a 2–4 km
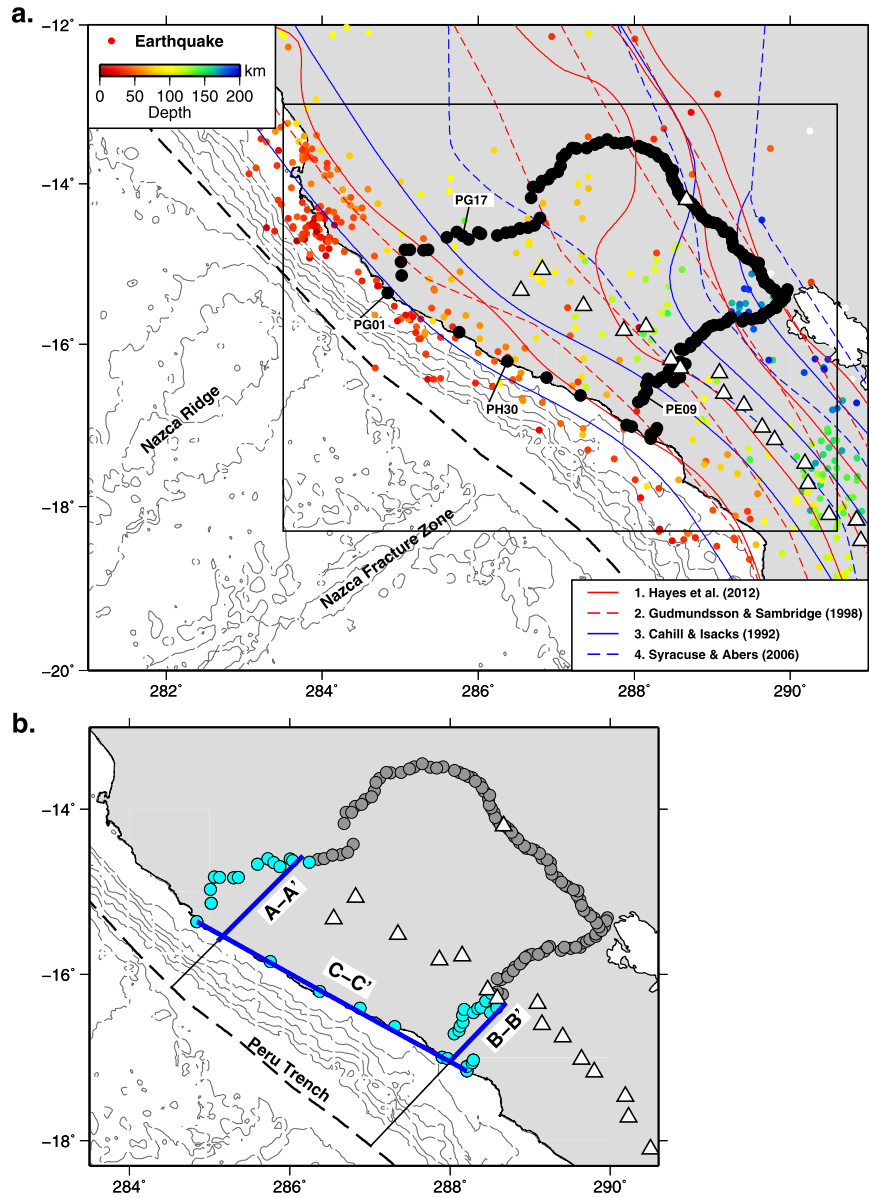
Fig. 2. Stations, profiles for imaging, and top-of-slab depth models. a. Four previously published slab models constrained by regional seismicity. Each line represents 50 km depth interval slab contours of the models (1: Hayes et al. (2012); 2: Gudmundsson and Sambridge (1998); 3: Cahill and Isacks (1992); 4: Syracuse and Abers (2006)). Note the trench location (black dashed line) marks 0 km slab depth. The slab depth down to 200 km is plotted. Unrelocated seismicity from earthquake catalog (NEIC; 2009–2012) is plotted as dots, color-coded by depth. b. Profiles for imaging. The stations used in the analysis are shown in cyan color, and three profiles (A–A′, B–B′, and C–C′) shown in blue solid line. (For interpretation of the colors in this figure, the reader is referred to the web version of this article.)

thick very low velocity channel is seen above the subducting crust.

2.1. Nazca Ridge

The upper plate tectonics of the southern Peruvian margin (from 2°S to 15°S) is closely linked with the subduction of the aseismic Nazca Ridge, a large seamount-range with ∼1.5 km topographic high (Clift et al., 2003). The ridge has entered the Peru Trench in the north (at 8°S) about 8 Ma (Cande, 1985) and migrated south about 800 km to its present position (Fig. 1). It currently intersects the trench ∼200 km north-east of where the Nazca slab is starting to flatten, with the convergence rate of about 7.1 cm/yr (DeMets et al., 2010). Unlike the flat subduction case in central Chile where the Juan Fernandez Ridge is subducting, the dip angle of the Nazca slab does not return to normal (see contour lines in Fig. 2) after the ridge has passed.

Whether the Nazca Ridge has sufficient buoyancy by itself to sustain the flat segment of about 800 km has been questioned by previous studies (e.g., van Hunan et al., 2002; Skinner and Clayton, 2013). Numerical modeling of the subduction of the moderate-size ridge suggests that the subduction process does not result in major changes of slab dynamics and magmatic activity compared to normal subduction (Gerya et al., 2009). Recent dense array data analysis further suggests that the ridge does not appear to contribute to shallowing of the subduction dip angle of the Nazca slab (Phillips and Clayton, 2014). The South-American westward absolute plate motion (van Hunan et al., 2002) may be an important effect for the creation of the Peruvian flat slab. In addition, considering an enigmatic case of the flat subduction in Mexico, the changes in the subduction dynamics through a change in mantle wedge viscosity by the slab dehydration process should be taken into account (Manea and Gurnis, 2007; Kim et al., 2013).

The surface of the Nazca Ridge is imaged to be quite rugged, featuring many seamounts that penetrate the sediment cover (Hampel et al., 2004; Krabbenhoft et al., 2004). The thickness of the sediment layer is thin but variable, and sporadically missing along the margin (from 8°S to 17°S) (Krabbenhoft et al., 2004). The total thickness of the sedimentary section atop the Nazca Ridge at a drill site 1237 (Fig. 1c) is estimated at 280–300 m based on site survey seismic profiles (Mix et al., 2003). The seismic record shows well-stratified reflective layers, which clearly delineate both sediment surface and top layer of the basement, which may be either basalt or lithified sediment (Mix et al., 2003). Furthermore, strong amplitudes in the reflection profile (Krabbenhoft et al., 2004) may originate from a high P-wave velocity contrast across the plate boundary indicating the presence of a subduction channel. The velocities of the sedimentary layers are quite low (∼1.6–3.0 km/s; Krabbenhoft et al., 2004). These offshore results infer strong impedance contrast across the interfaces, and such layers can be also imaged with teleseismic converted phases onshore.

A rough seafloor associated with the Nazca Ridge may cause lower interseismic coupling rate in southern Peru and thus aseismic creep in the interseismic period (Perfettini et al., 2010; Chlieh et al., 2011). It may act as a permanent barrier, stopping the propagation of large ruptures (Wang and Bilek, 2014).

2.2. Nazca fracture zone

Roughly 450 km south of the Nazca Ridge, the Nazca fracture zone, a dextral transform–fault structure, is present (Fig. 1), and its dimension is comparatively smaller than the Nazca Ridge. The fracture zone has a depressed valley structure (∼1.2 km deep) along the fault line. Such structure may trap more sediment and also allow more contact with the seawater. Despite the bathymetric irregularities and this potential source of hydration near the plate interface, the style of the subduction appears to be normal (30° estimated from the teleseismic receiver function analysis (Phillips et al., 2012)).

Robinson et al. (2006) linked the fracture zone as a rupture barrier of the 2001 Arequipa earthquake (Fig. 1b). Inversion results from the geodetic measurements suggest a relatively lower interseismic coupling in this region, compared to the region farther south, but higher than the region close to Nazca Ridge (Chlieh et al., 2011), supporting previous observation (Robinson et al., 2006). However, Chlieh et al. (2011) argue that this region can also permit great ruptures as happened in 1604 and 1868.

3. Geophysical datasets

3.1. Heat flow, gravity, and geoid

The flat slab region is characteristically considered to be a cool back-arc mantle (Currie and Hyndman, 2006). In the flat slab region in southern Peru, the heat flow near the coast is 30–40 mW m^{-2}, typical of fore arcs, but it is atypically low for a back arc, ∼50 mW m^{-2} (Fig. 1c; Pollack et al., 1993). In addition, there is no active volcanic arc in this region, suggesting that the mantle is relatively cool. The absence of volcanism is explained by the disappearance of the hot mantle wedge with the decreasing dip angle of the slab. The absence of the contact of the hydrated subducted crust with the overlying mantle wedge precludes partial melting and associated volcanism. As the dip angle of the subducting slab increases towards south, the magmatism starts to appear, and as expected, the higher heat flow values are observed in the back arc (Fig. 1c; Pollack et al., 1993).

Density anomalies generally induce gravity and geoid anomalies. In particular, geoid anomalies, at wavelengths of several thousand kilometers, are indicators of internal density anomalies driving mantle convection and thus plate motion. In southern Peru, bathymetric anomalies atop the Nazca Plate are well associated with positive density anomalies (Fig. 1d), and they may be related to the presence of deep negative temperature anomalies. Whereas, there is no obvious correlation between the bathymetric anomalies and observed geoid anomalies (Fig. 1e). Lower geoid trough along the Peru Trench may be due to the dynamically sinking of the slab. Negative density anomalies are clearly observed due to negative surface topography associated with the trench. The Peru Trench is an erosive margin (Clift et al., 2003), with very little sediment fill (Krabbenhoft et al., 2004), thus light crustal materials entrained within the subduction complex are not likely a significant contributor to the gravity anomalies (Fig. 1d).

3.2. Regional seismicity

Southern Peru is an ideal location to study the relationship between large-magnitude earthquake and structural subduction zone heterogeneity. In particular, long earthquake catalogs along with the geodetic measurements are available to examine changes in rupture behavior of the large-magnitude earthquakes. Earthquakes in 1942 ($Mw = 7.9$–8.2) and 1996 ($Mw = 7.7$) both occurred along the plate interface at the region where the Nazca Ridge subducts (Fig. 1b; Bilek, 2010, and references therein). The significant rupture propagation and moment release to the south, away from the Nazca Ridge (Swenson and Beck, 1996), was found. The 2001 event ($Mw = 8.4$; Bilek, 2010, and references therein) is notable because of the suggestion of a barrier during rupture (Robinson et al., 2006). Robinson et al. (2006) linked this barrier and resulting rupture complexity to a bathymetric high associated with the subducting Nazca fracture zone.

Earthquake locations typically provide the first-order estimate of the oceanic slab geometry. Exploiting the relatively long earthquake catalog, various research groups previously proposed slab geometry models by examining locations of the earthquakes (Fig. 2). The sparsity of the regional seismic network however yields a significant disagreement in such models. Specifically, the iso-depth contour lines for the Nazca slab at 50 and 100 km show the least coherence (Fig. 2). Furthermore, the correlation between the location of the active volcanic front and corresponding slab depth is neither clear nor consistent between the models (Fig. 2). The location of the plate interface beneath/near the station is most directly resolved with teleseismic converted phases recorded from the densely spaced stations.

4. Data analysis and methods

4.1. Data processing and teleseismic converted phase analysis

We use teleseismic scattered wavefields recorded from three passive seismic lines in southern Peru to resolve major boundaries such as the top and bottom interfaces of the subducting Nazca crust. Three-component broadband seismometers were deployed in four linear arrays, two of which are nearly perpendicular and two are parallel to the strike of the Peru Trench (Fig. 2). Each line operated for approximately two years. In this study, we only use selected stations from three profile lines (PE, PG, and PH lines; Fig. 1a), shown in Fig. 2. We identify P-wave arrival of teleseismic earthquakes (with magnitude greater than 5.5 and epicentral distances between 30 and 95; Fig. 3) and then time-window to 90 s to ensure P and P coda phases. Retrieved data are then bandpassed from 0.01 to 1.0 Hz prior to the rotation in the L–Q–T coordinate system. See Supplementary Data for a description of calculating radial receiver functions (RFs).

Identification of strong and sharp amplitudes of the P-to-S converted phase (hereafter, Ps) is crucial in this analysis. For the RF,
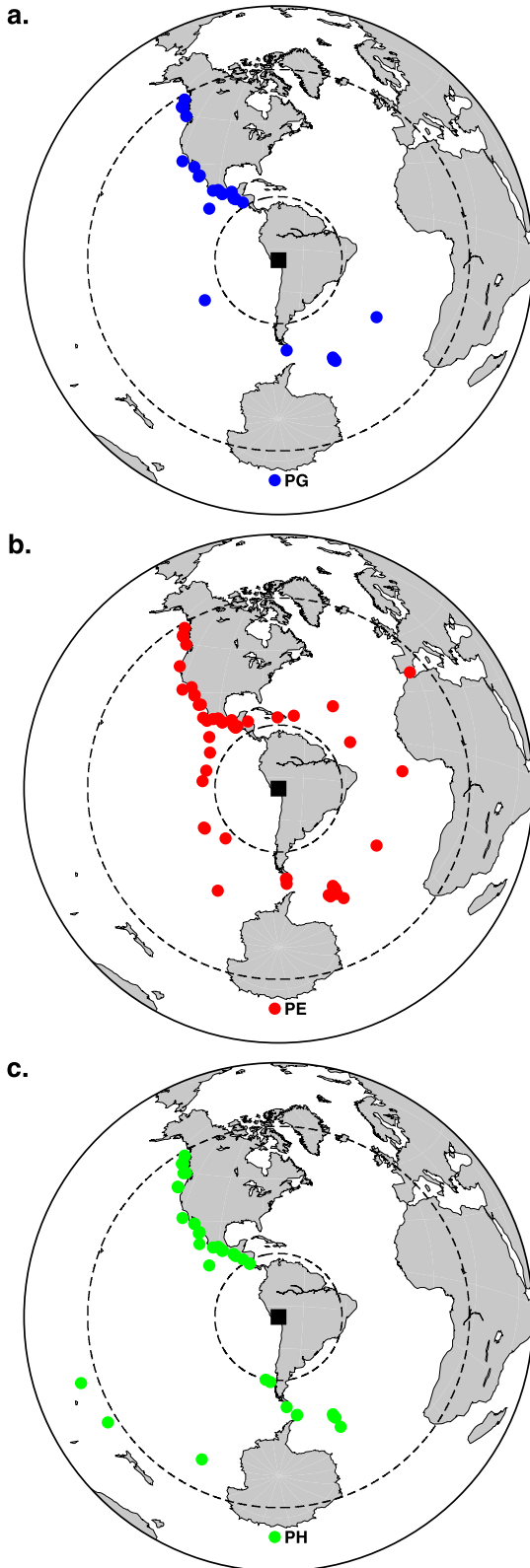
Fig. 3. Teleseismic earthquakes for receiver functions (RFs) and migration. a. Event distribution for PG line (Fig. 1a). The 29 earthquakes are selected away from the point (longitude of −74.4°, latitude of −15.1°) of the profile A–A′ (Fig. 2b). b. Event distribution for PE line (Fig. 1a). The 54 earthquakes are selected between 30° and 95° away from the point (longitude of −71.9°, latitude of −16.8°) of the profile B–B′ (Fig. 2b). c. Event distribution for PH line (Fig. 1a). The 40 earthquakes are selected away from the point (longitude of −73.6°, latitude of −16.2°) of the profile C–C′ (Fig. 2b).

the amplitude of the conversion is imaged (e.g., Supplementary Figs. S1 and S2), and the peak of the RF pulse indicates the discontinuity interface with its polarity controlled by the impedance contrast across the discontinuity. We measure the amplitudes of the negative–positive pair in each RF, normalized by its maximum amplitude. Supplementary Fig. S2 shows example RFs computed at a single station in each seismic line, with top plate interface locations highlighted by an arrow. Each station has a minimum of 20 traces. The collection of the RF amplitudes for all the selected stations is used in the inversion, which we will describe in the following subsection.

In addition to the RF, we also apply the migration of the teleseismic scattered wavefields based on the 2-D Generalized Radon Transform (GRT) (Bostock et al., 2002, and references therein). The method assumes that the scattered wavefields are generated by volumetric perturbations in P and S wave velocities within a smoothly varying background velocity model (Supplementary Table S1). The 2-D GRT simultaneously inverts a combination of forward and backscattered (or reverberated) modes using analytical expressions for their travel times and amplitudes. The scattering modes are defined as the incident P wave forward scattered as an S wave (Ps); the free-surface-reflected P wave backscattered as a P wave (PpPp); the free-surface-reflected P wave backscattered as an S wave (PpPs); and the free-surface-reflected S wave backscattered as an Sv wave (PpSs|v) and Sh wave (PpSs|h). The four scattering modes (Ps, PpPs, PpSs|v, and PpSs|h) are sensitive to S wave velocity perturbations (dVs/Vs) and are combined to form a single composite image. As more migrated phases are stacked in, the artifacts due to cross-mode contamination (i.e., parallel echoes of the real structure) become attenuated while energy mapped to its correct depth is sharply imaged (e.g., Kim et al., 2012a). The dVs/Vs in all the migration images in Section 5 are shown with a red to blue color scale, which represents negative (slower) to positive (faster) velocity perturbations. Detailed method and its recent application to dense seismic array datasets in Mexican subduction zones are described in Kim et al. (2012a).

4.2. Receiver Function (RF) amplitude inversion

The amplitudes of the distinct negative/positive signature of the RF pulses are indicative of the conversion at the top and bottom interfaces of the subducting crust. Converted phase amplitudes and their time separation can be used to constrain shear wave velocity and density of the subducting crust and its thickness, respectively. The inversion capability using the RF amplitudes was previously demonstrated based on the linearized Zoeppritz equations assuming small incidence angles, which was suitable for conversions along the dipping portion of the oceanic crust in Mexico (Kim et al., 2010, 2012b). As discussed in Kim et al. (2010), the measured conversion amplitudes have strong sensitivity to S-velocity (Vs) and weak sensitivity to density over the limited range in slowness (0.04–0.08 s/km). The initial negative pulse mostly depends on the variation in Vs of the top interface of the upper portion of the oceanic crust (LVZ; Fig. 4), while the following positive pulse depends on the contrast in such quantity across the bottom interface of the lower oceanic crust (LOC; Fig. 4). We follow the same inversion step described in Kim et al. (2010), which is also summarized in Supplementary Data. The time separation of the amplitudes is used to invert for the thickness of the oceanic crust (thickness of LVZ and LOC).

4.2.1. Input velocity model for inversion and uncertainty in velocities

The inversion requires a reference model for both velocities and density, so we construct models for the inversion based on offshore/onshore seismic and IODP results (e.g., ANCORP Working Group, 2003; Krabbenhoft et al., 2004; Mix et al., 2003), waveform
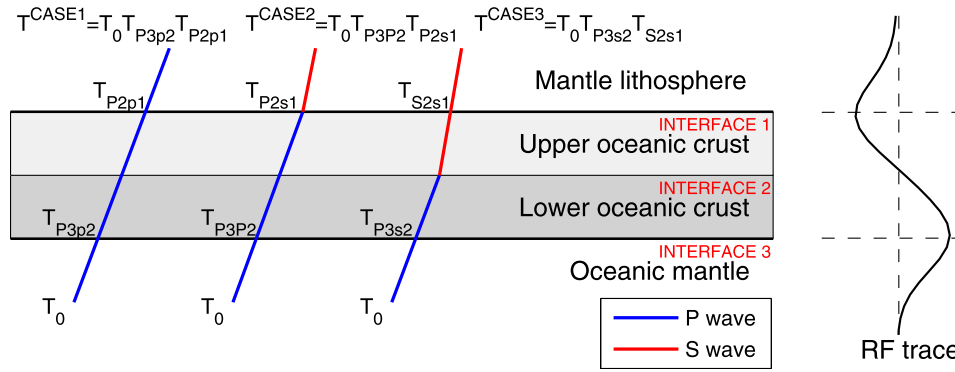
Fig. 4. Schematic showing transmitted responses at top and bottom interfaces of the oceanic crust. This figure is a modified version of Fig. 13 in Kim et al. (2010). The peak of the negative receiver function (RF) pulse is obtained at the interface 1 between the mantle wedge and the low-velocity upper oceanic crust (LVZ); the peak of the positive RF pulse at the interface 3 between the lower oceanic crust (LOC) and the oceanic mantle. See Supplementary Data for details.

modeling results (Phillips et al., 2012; Phillips and Clayton, 2014), and tomography (Phillips et al., 2012), sampling the subducting Nazca slab along the subduction margin. We vary the range of Vp of upper plate crust between 6.0–6.5 km/s, the mantle wedge between 6.5–7.0 km/s, and the oceanic mantle between 8.0–8.5 km/s (Supplementary Table S2), and test the sensitivity of the inversion to account for the uncertainties in the velocities.

In particular, we require P-wave velocities (Vp) of both upper and lower portion of the subducted crust (LVZ and LOC, respectively) in the inversion, and these values are later used again to compute P-to-S velocity ratios (Vp/Vs) and Poisson's ratios. Since the Vp/Vs strongly depends on the mean rheology of the oceanic crust, we vary the range of Vp of LVZ between 5.0–6.0 km/s, and LOC between 6.7–7.3 km/s (Supplementary Table S2), following the values given by offshore seismic results (Krabbenhoft et al., 2004). We note that in the inversion we did not take into an account of the Vp of the LVZ and LOC changing with depth due to the metamorphisms of its materials. Another source of uncertainty may come from the RF amplitude change with the slab dip. However, uncertain Vp values of LVZ and LOC affect the inversion results considerably than the amplitude change by the slab dip.

Since we assume seismic velocities except values for subducted crustal layer (Supplementary Table S2) in the inversion, we provide absolute Vs rather than the perturbations to directly relate to the mineralogical and petrological phase estimates. We display inversion outputs in Vs plotted against Vp/Vs (e.g., Figs. 5c, 6c, and 7b). The variations in Vs can be caused by changes in temperature, bulk composition, hydration state, or partial melting within the subducted crust or by a combination of these factors. These listed factors can cause a non-linear effect on Vp/Vs, and hence we use a range of velocities.

5. Seismic images and inversion results

We present both RF and migration images (Figs. 5, 6, and 7) spanning the three profiles, as shown in Fig. 2b. Both methods constrain depths to major boundaries such as the top and bottom interfaces of the subducting Nazca crust, from direct conversion (Ps) and reverberations. By examining the converted amplitudes from images and performing the amplitude inversion, we constrain plate interface properties, such as seismic velocities with ranges of uncertainty.

5.1. Flat slab subduction zone

The images (Figs. 5a and 5b) show a low-velocity oceanic crust with a ~20° dip at 25 km depth near the Peruvian coast (120 km from the trench). The dip of this low velocity layer transitions to

flat at ~80 km depth at 220 km from the trench. The negative RF pulse (Fig. 5b, blue dashed line) marks the top of the subducted Nazca Plate, while the positive (Fig. 5b, red dashed line) marks the bottom interface of the oceanic crust. This is the region with no arc magmatism. We find a considerable disagreement between our estimate of the dipping angle (Fig. 5a, solid line) and Slab1.0 model constrained from seismicity (Fig. 5a, dashed line; Hayes et al., 2012).

The velocity perturbations of the low-velocity layer shown in the migration image are estimated to be $dVs/Vs = \sim2.0\text{–}6.8\%$ (Fig. 5a). The strength of both negative and positive RF amplitudes weakens significantly toward northeast (Fig. 5b; horizontal location >270 km). Thus, we only show the RF image up to 300 km from the trench (Fig. 5b) and the migration image up to 270 km (Fig. 5a).

The inversion yields Vs of ~3.3–3.8 km/s and Vp/Vs of ~1.64–2.03 for upper oceanic crustal depth ranges between ~45 and 80 km (Fig. 5c). In the inversion, Vp for the LVZ and LOC are prescribed as 5.5 km/s and 7.0 km/s, respectively. At the depth range before the slab is flattened (depth <80 km), both Vs and Vp/Vs estimates for the LVZ are highly varying, and tend to be lower (3.3–3.6 km/s) and higher (1.8–2.03), respectively (Fig. 5c, colored circles). Note for several points corresponding to the region where the slab is flattened (depth ≥80 km; Fig. 5a, horizontal location = 220 km), Vp/Vs estimates are relatively high (>1.8; Fig. 5c, colored circles). However, Vs values gradually decrease with some deviations in the region farther inland (Fig. 5a, horizontal location >250 km). Both Vs and Vp/Vs estimates are sensitive to the Vp of the LVZ layer and the medium above (mantle lithosphere, ML). By increasing and decreasing the Vp of the LVZ, both estimates shift up and down, respectively (Fig. 5c, lighter gray shaded area). By increasing and decreasing the Vp of the ML, both estimates shift to lower-right and upper-left, respectively (Fig. 5c, thick, darker gray line).

Compared to broadly scattered, linear-trend data for LVZ (Fig. 5c, colored circles), the data points for LOC (Fig. 5c, colored squares) are tightly bounded in Vs and Vp/Vs domain, and can be divided into two groups. The first group are bounded in $Vs = 4.1\text{–}4.3$ km/s and $Vp/Vs = 1.72\text{–}1.79$, and lie close to velocities of mineral phases like amphibole, lawsonite, and zoisite. Based on this seismic observation, except for amphibole, we cannot distinguish whether such two mineral phases coexist or not, due to their similar velocities at the LVZ depth of ~50–100 km. The second group are tightly bounded in $Vs = 4.4\text{–}4.6$ km/s and $Vp/Vs = 1.61\text{–}1.66$, and gabbro is also capable of explaining the data for LOC with the uncertainty range. These values are characterized by lower Vs than those of pyroxene and eclogite. Both Vs and Vp/Vs estimates are sensitive to the Vp of the LOC layer and
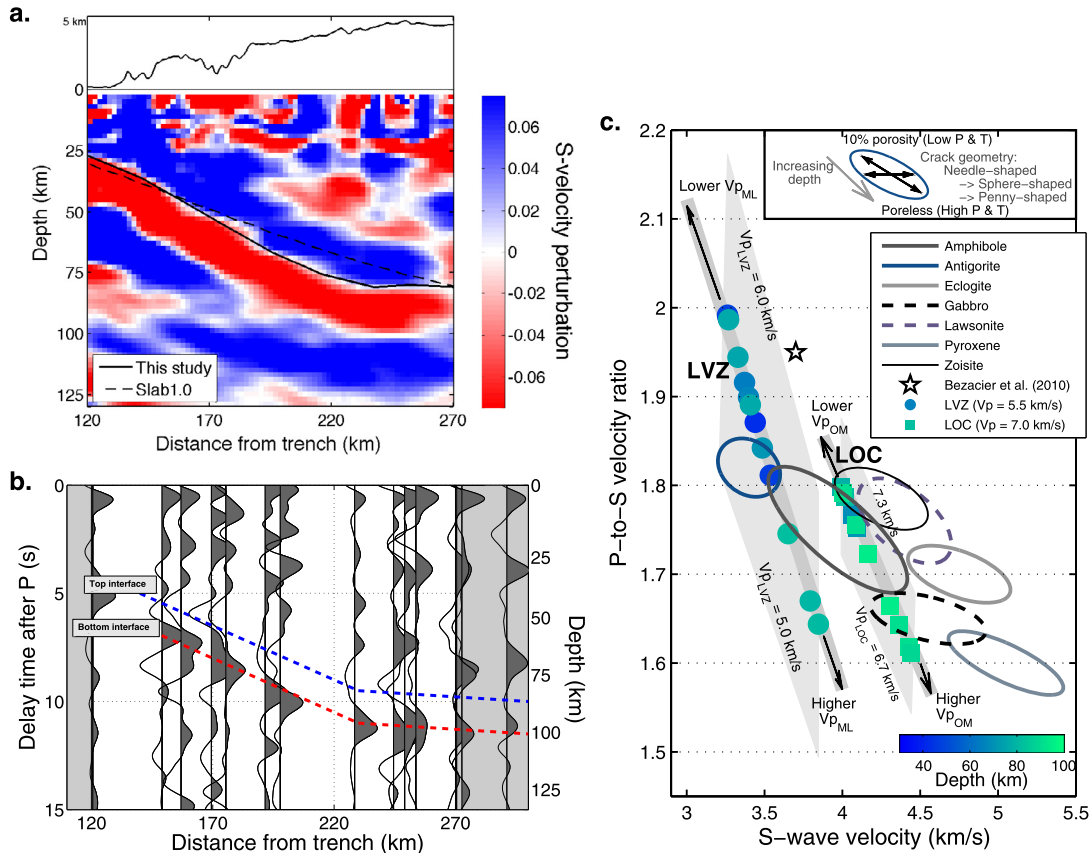
Fig. 5. Seismic images along the projection line A–A′, showing flat Nazca slab. The zero km point coincides with the trench location. a. Migration image with interpretation lines and topography on top (vertical exaggeration by 6.0). A black solid line represents a top interface of the Nazca crust from the image. We include the top interface of the slab from Slab1.0 model (Hayes et al., 2012) as a dashed line for comparison. b. Stacked RFs using teleseismic earthquakes in all backazimuths (Fig. 3a) and a subset of the stations in the PG line (Fig. 2b). Top and bottom interfaces of the Nazca oceanic crust are highlighted as dashed lines in blue and red, respectively. c. Calculated P-to-S velocity ratio (Vp/Vs) versus S-wave velocity (Vs) at depth ranges of 30–100 km for the profiles A–A′. The data points (shown in colored circles and squares) are calculated using Vp of mantle lithosphere (ML) as 6.75 km/s, oceanic mantle (OM) as 8.25 km/s, LVZ as 5.5 km/s, and LOC as 7.0 km/s (Supplementary Table S2). The color scale shows the average of the depth of the top- and bottom-interfaces of the oceanic crust. A lighter gray area shaded in the background of the data is obtained by varying Vp of the LVZ or LOC. A thick, darker gray line is obtained by varying Vp of ML or OM. Ellipses in different line and color properties represent candidate mineral and rock phases. The elasticity data for the mineral phases and rocks used in the calculation are provided in Kim et al. (2012b). Also, in the calculation, we assume pressure (P) of 1.0 GPa and temperature (T) of 450 °C at 40 km and 2.0 GPa and 700 °C at 120 km. The lower-right part in each ellipse represents poreless mineral or rock phases in high P and T conditions, and the upper-left portion represents the phases with various shape-crack (needle, sphere, or penny) water-filled inclusions of maximum porosity of 0.1 in low P and T conditions. Different crack geometry affects seismic velocities, and each ellipse in this figure is drawn to encompass all velocities. The data point shown as a star indicates a value computed for Vs at a 30° incidence angle between the seismic ray path and foliation plane of Cuba serpentinite at room P and T condition (Bezacier et al., 2010). See more details in Supplementary Data. (For interpretation of the colors in this figure, the reader is referred to the web version of this article.)

the medium below (oceanic mantle, OM). The uncertainty trend appears similar to the case for LVZ.

5.2. Normal-dipping slab subduction zone

The images (Figs. 6a and 6b) show a low-velocity oceanic crust with a ∼30° dip at 40 km depth near the Peruvian coast (horizontal location (from trench) = 150 km). Our estimate of the dipping angle agrees quite well with the previous estimates from the RFs (Phillips et al., 2012) and seismicity (Fig. 6b, dashed line; Hayes et al., 2012). The velocity perturbations of the low-velocity layer are estimated to be dVs/Vs = ∼2.5 to ∼5.0% (Fig. 6a). We only show both RF and migration images up to 270 km from the trench (Figs. 6a and 6b) because we observe that the strength of the negative RF amplitudes weakens significantly toward northeast (Fig. 6a, horizontal location >240 km). In addition, the positive RF amplitudes, converted signals from the oceanic Moho, are imaged clearly (Fig. 6b, red dashed line), and such features extend for ∼20–30 km farther deep (compared to the trend for the negative amplitudes), as also observed by Phillips et al. (2012).

The inversion from the data sampling normal-dipping LVZ yields Vs of ∼3.4–4.2 km/s and Vp/Vs of ∼1.61–1.98 at depth of

∼30–80 km (Fig. 6c). In the inversion, Vp for the LVZ and LOC are prescribed as 5.5 km/s and 7.0 km/s, respectively. Compared to the results for the flat dipping segment (Fig. 5c, colored circles), seismic velocities for the LVZ (Fig. 6c, colored circles) are comparatively elevated by ∼10–20%. Consequently, both Vp/Vs and Poisson's ratios (Fig. 6c) tend to be lower than those from the flat slab region (Fig. 5c). The dominant mineral phase is observed to be amphibole in dipping upper crust (Fig. 6c). Seismic anisotropy from the preferentially oriented serpentinites (Bezacier et al., 2010) may also explain observed data points within the uncertainty range (Fig. 6c). The data points for the LOC (Fig. 6c, colored squares) at the depth of ∼40–95 km, on the other hand, suggest dominant gabbroic composition in this region. Both Vs and Vp/Vs estimates for LVZ and LOC are sensitive to the Vp of the LVZ and LOC, and the Vp of ML and OM, and their uncertainty ranges are shown in Fig. 6c.

5.3. Slab-dip transition zone between the flat and normal slab subduction

We only show RFs computed from seven stations nearest to the Peruvian coast (Fig. 7a) along the profile C–C′ (Fig. 2b) since
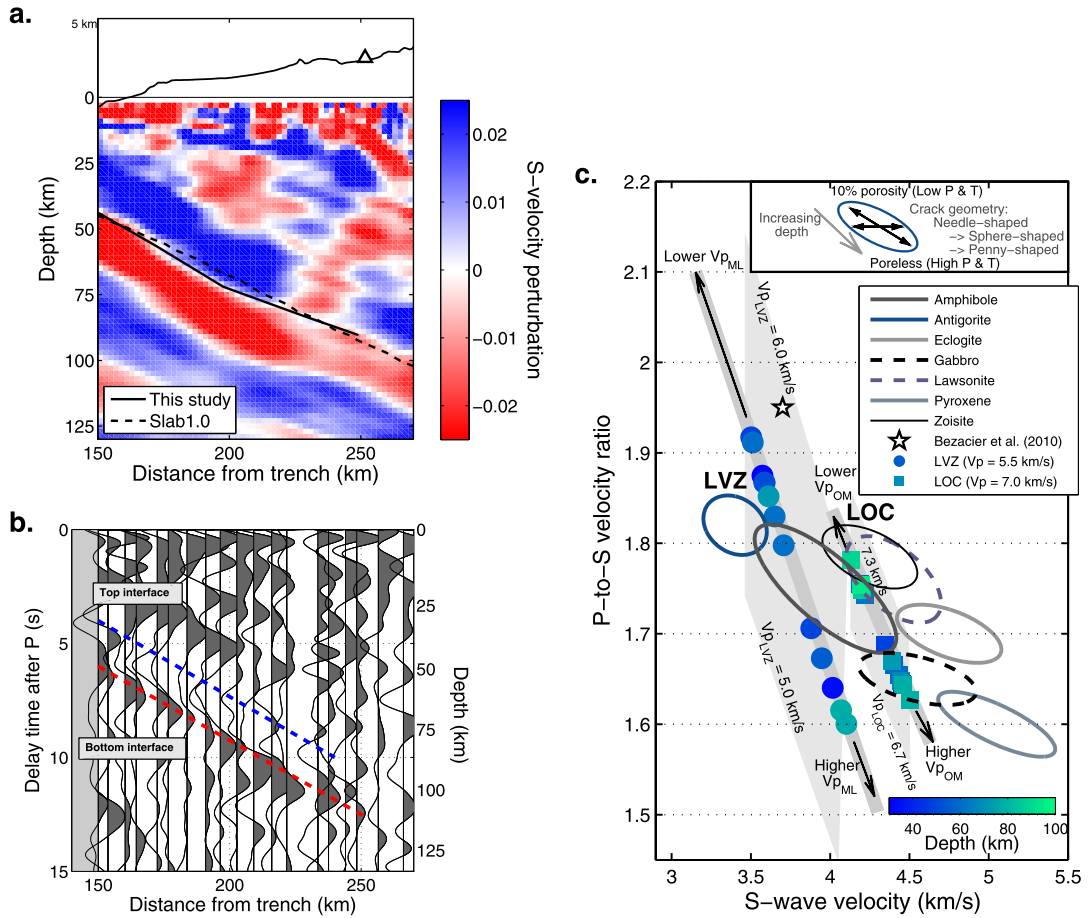
Fig. 6. Seismic images along the projection line B–B′, showing normal-dipping Nazca slab. The zero km point coincides with the trench location. a. Migration image with interpretation lines and topography on top (vertical exaggeration by 6.0). Arc front location is indicated as a triangle. A black solid line represents a top interface of the Nazca crust from the image. We include the top interface of the slab from Slab1.0 model (Hayes et al., 2012) as a dashed line for comparison. Stacked RF traces between 0 and 90 km (region enclosed in a black (thinner) dashed box) are separately calculated and shown in a panel b. b. Stacked RFs using teleseismic earthquakes in all backazimuths (Fig. 3b) and a subset of the stations in the PE line (Fig. 2b). Top and bottom interfaces of the Nazca oceanic crust are highlighted as dashed lines in blue and red, respectively. c. Calculated Vp/Vs versus Vs at depth ranges of 30–100 km for the profiles B–B′. The data points (shown in colored circles and squares) are calculated using Vp of mantle lithosphere (ML) as 6.75 km/s, oceanic mantle (OM) as 8.25 km/s, LVZ as 5.5 km/s, and LOC as 7.0 km/s (Supplementary Table S2). The color scale shows the average of the depth of the top- and bottom-interfaces of the oceanic crust. A lighter gray area shaded in the background of the data is obtained by varying Vp of the LVZ or LOC. A thick, darker gray line is obtained by varying Vp of ML or OM. See caption of Fig. 5c and Supplementary Data for ellipses and a star drawn. (For interpretation of the colors in this figure, the reader is referred to the web version of this article.)

the teleseismic migration requires more denser station spacing. The top and bottom interfaces of the low-velocity oceanic crust are marked with blue and red arrows, respectively (Fig. 7a). Since these stations are located near the coast, the signal-to-noise ratio (SNR) (especially from four stations in PH line (Fig. 1a)) is relatively low. Although a lower frequency band in the data processing (filtering) step may improve the SNR for several stations, we use the same high frequency band as other profile data because conversions at the top and bottom interfaces are clear (Fig. 7a), and thus can be usable in the inversion. From the RFs, a thickness of the continental crust near the coast varies between ∼25 and 50 km from NW to SE along the profile C–C′ (Fig. 7a). A thickness of the subducted oceanic crust is estimated as ∼8–14 km.

The inversion yields Vs of ∼2.5–3.0 km/s and Vp/Vs of ∼1.9–2.2 for upper oceanic crustal depth ranges between ∼25 and 50 km (Fig. 7b, colored circles). These values cannot be explained with their uncertainty ranges by any candidate phase used in this study. The data points for the LOC at the depth of ∼30–65 km (Fig. 7b, colored squares), on the other hand, suggest the presence of amphibole. Considering the uncertainty range in Vp of LOC and OM, the data points for the LOC also lie marginally close to velocities of mineral phases like lawsonite, and zoisite, and close to rock phase

like gabbro. An average value of Vp/Vs of the LOC is estimated as 1.733 (Fig. 7c).

Along the C–C′ at the plate interface depth of 25–50 km, we observe much higher Vp/Vs (>2.0) and Poisson's ratio (>0.33) due to lower Vs for LVZ near the slab flattening region (Fig. 5c, colored circles), compared to the values in the normal slab-dip region (Vp/Vs < 2.0) (Fig. 7c). The estimates for LVZ in the slab-dip transition zone are variable, but observed higher than the normal slab-dip region (Fig. 7c).

Lastly, we note that density is not as good of an indicator to distinguish compositional models from the seismic dataset because the inversion is more sensitive to the perturbation in shear velocities rather than density (Kim et al., 2010, 2012b). The inverted densities for all three profile regions show values between 3200 and 3400 kg/m³, and the values are depth-dependent.

6. Discussion

Strong (negative) amplitudes in our RF images (Figs. 5b, 6b, and 7a) originate from a high velocity contrast across the plate boundary indicating the presence of a subduction channel (shear zone or fault zone) (e.g., Krabbenhoft et al., 2004), hydrous minerals (e.g., Kim et al., 2010), and/or high pore fluid pressure (e.g.,
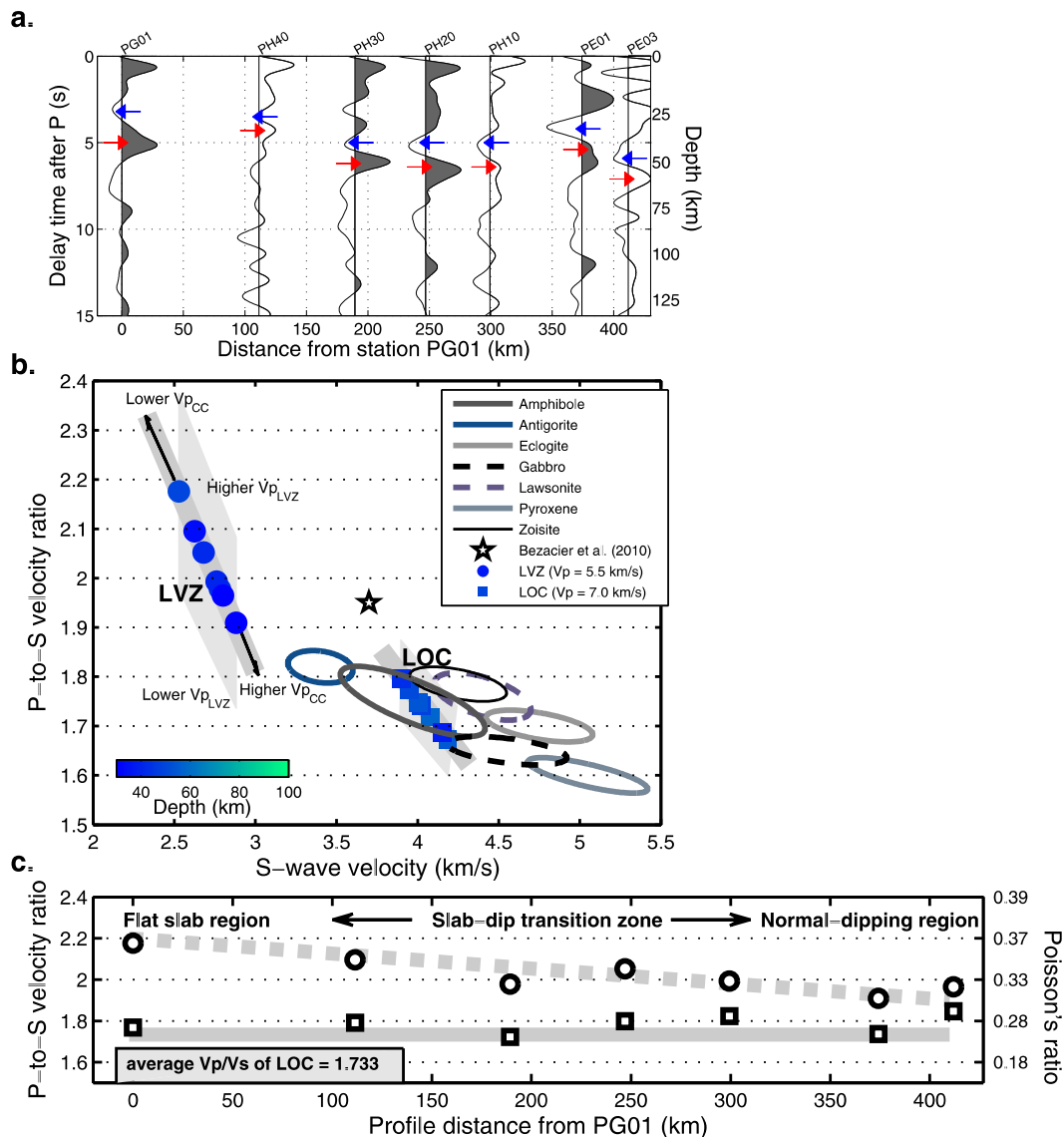
Fig. 7. Seismic images along the projection line C–C′, showing the along-arc change in Nazca Plate interface properties. a. Stacked RFs along the projection line C–C′. The RFs are computed using teleseismic earthquakes in all backazimuths (Fig. 3c) and all stations in the PH line, PG01, PE01, and PE03. Top and bottom interfaces of the oceanic crust are marked by blue and red arrows, respectively. b. Calculated *Vp/Vs* versus *Vs* at 25–65 km depth. The data points (shown in colored circles and squares) are calculated using *Vp* of continental crust (CC) as 6.25 km/s, oceanic mantle (OM) as 8.25 km/s, LVZ as 5.5 km/s, and LOC as 7.0 km/s (Supplementary Table S2). The color scale shows the average of the depth of the top- and bottom-interfaces of the oceanic crust. A lighter gray area shaded in the background of the data is obtained by varying *Vp* of the LVZ or LOC. A thick, darker gray line is obtained by varying *Vp* of CC or OM. See caption of Fig. 5c and Supplementary Data for ellipses and a star drawn. c. Obtained *Vp/Vs* and Poisson's ratio, plotted against the profile distance from the station PG01. Circles represent the data for LVZ, and squares the data for LOC. A solid and dashed gray line show the trend of inversion results from LVZ and LOC data, respectively. An average value of *Vp/Vs* of the LOC is estimated as 1.733. (For interpretation of the colors in this figure, the reader is referred to the web version of this article.)

Audet et al., 2009). The density contrast between the ridge (including a thin sedimentary section) and overlying material (Mix et al., 2003) can also explain such large amplitudes. Similarly, strong amplitudes (so-called 'bright spot') are typically seen in seismic reflection images beneath accretionary prisms offshore. Such imaged features can arise from any interface with a strong lithology-contrast and/or a contrast in the Poisson's ratio, possibly due to the presence of fluid lenses within the subduction channel. This bright spot zone typically appears discontinuous, partly because of much higher frequency filters used in processing offshore seismic data and lower spatial resolution than the onshore data, suggesting heterogeneous fluid distributions within the shear zone. In contrast, onshore seismic images (e.g., Figs. 5a and 6a; Kim et al., 2012a, 2014) show more smooth and continuous low-velocity feature at the top of the plate.

Composition and dynamics of the subducting slab and overlying mantle wedge are strongly dependent on temperature and water content. Seismic imaging generally provides an instantaneous image of average fluid contents and does not constrain the origin of the fluids. In this section, based on our images we first address seismic properties of the observed low-velocity layer in two different regions. Then, we discuss (1) processes of the low-velocity (shear) deformation zone near the plate interface, and (2) the role of water in mantle, in changing rheological and seismological properties, and subduction dynamics in southern Peru. We discuss these points by comparing with Mexico subduction zone system, which involve the slab-dip transition between flat and normal subduction (Kim et al., 2010, 2012b, 2013).

6.1. Seismic properties of the dipping low-velocity layer

In the subduction system, the presence of a dipping low-velocity layer at depths of about 40–150 km likely associated with the subducted oceanic crust (Abers, 2005). Our seismic images (Figs. 5a–b, 6a–b, and 7a) show clear low-velocity features, and obtained velocity estimates suggest the presence of hydrous minerals (Figs. 5c, 6c, and 7b). In particular, the amphibole-dominated mineralogy in LVZ (Fig. 6c) suggests that it can be an important host for H_2O. The amphibole-bearing oceanic crustal assemblage is also seen in central Andes (21°S) (ANCORP Working Group, 2003), and in southern Mexico (Kim et al., 2012b).

At high pressures, hydrated basalt and gabbro convert to higher-velocity eclogite, which can no longer be distinguished from mantle peridotite seismically (Hacker et al., 2003). Based on our image showing the shallowly dipping low-velocity layer (Figs. 6a and 6b), the depth of ∼80–100 km marks the onset of high-pressure metamorphic facies, such as eclogite, leading to a density increase within the subducted oceanic crust. This can also explain arc volcanism in this region (arc location, shown as a triangle in Fig. 6a). Expelled free water should migrate directly upward due to buoyancy into the overlying mantle wedge. Because the presence of water substantially lowers the melting temperature of the mantle peridotite, the water eventually triggers the mantle melting to generate arc volcanism.

Our RF image for the flat subduction zone along the profile A–A′ shows that the strength of the negative RF amplitudes weakens significantly toward northeast at 270 km from the trench (Fig. 5b) in the trench-normal direction. Weaker Ps conversions observed here (or the disappearance of the low-velocity layer; Figs. 5a and 5b), however, do not constrain the depth of eclogitization. The low-velocity signal near the plate interface weakens and further disappears for ∼100 km and reappears in the flat segment (Ma and Clayton, 2014). Such significant amplitude variation is not yet clear, but may be related to irregular bathymetric feature due to the subduction of the ridge (Ma and Clayton, 2014).

Furthermore, there is a considerable slab-dip discrepancy between our result and the model from seismicity (Hayes et al., 2012) in the flat slab subduction zone. Such slab-dip discrepancy may arise from the relatively low occurrence rate of large-magnitude earthquakes constrained in the model (Hayes et al., 2012), compared to the region in the south (profile B–B′ in Fig. 2) and other slab dipping segments along the Peru Trench. This is similar to central Mexico, where the top interface of the horizontal slab cannot be defined by the seismicity alone (Kim et al., 2010).

Lastly, the data points for LOC for all three profile regions from the inversion suggest that LOC is generally homogeneous in composition, and gabbro is capable of explaining the LOC data. Denser rocks such as pyroxene and eclogite are characterized by higher Vs than our estimates for LOC. This may also imply that a degree of fluid alteration is low in LOC.

6.2. Variations in frictional properties along the plate interface

We observe elevated Vp/Vs (and Poisson's ratio) due to lower Vs estimates in the flat slab region, compared to the values in the normal slab-dip region (Fig. 7c). Different seismic velocities and Vp/Vs in those two regions, downdip of the seismogenic zone, may suggest different hydration degrees and/or dominant composition near the plate interface. Lower Vs in the flat slab region (Fig. 5) can be indicative of fluid-rich state of the plate boundary (i.e., greater hydration degree and/or enrichment of hydrous phases), which can promote lower friction and interseismic creeping-states along the Peruvian margin, as evidenced from geodetic measurements (Perfettini et al., 2010; Chlieh et al., 2011). In the case for central Mexican flat subduction, some parts of the LVZ at ∼45 km

depth correspond to anomalously low Vs (2.4–3.4 km/s) and thus higher Vp/Vs (up to 2.1) and Poisson's ratio (Kim et al., 2010). Such lower Vs indicate that a top portion of the flat slab is hydrous, and the presence of frictionally weak phases such as serpentine and talc in the LVZ may reduce tectonic coupling between overriding and subducting plates (Kim et al., 2010, 2012b, 2013). The evidence of high H_2O content near the flat interface in southern Peru may originate from the subducting ridge and/or subduction channel. The subduction of the ridge may give rise to a weaker coupling state between subducting and overriding plates, which are evidently seen from lower occurrence rate of intraslab events near the flat segment. In addition, the variability of subducted materials (e.g., thickness and composition) in the subduction channel affects the interplate coupling states of the subduction thrust zone.

The elevated pore fluid pressure within the hydrous, frictionally weak channel can be also an important to factor to lower Vs. In particular, the inversion for the C–C′ profile, sampling the shallower depth of the subducting Nazca crust, yields Vs of ∼2.5–3.0 km/s and Vp/Vs of ∼1.9–2.2 at depth ranges between ∼25 and 50 km (Fig. 7b). These estimates, even accounting for the uncertainty ranges, cannot be explained by any candidate phase. Elevated pore fluid pressure may be responsible for the lower velocities observed (Christensen, 1984). The influence of the pore pressure on seismic velocities is, however, expected to diminish with depth, and thus we expect that it is unlikely to be significant at LOC and farther away from the seismogenic zone. In addition, other explanations could include free fluids, fabric development, as well as a lack of complete elasticity data for all candidate phases, including phase transitions and elastic anisotropy.

At the flat slab region in Peru, the Vs near the top plate interface are lowered by ∼20–40%, (thus resulting in higher Vp/Vs up to 2.1) and by ∼20–30% for < ∼4% porosity in Cascadia (Audet et al., 2009). In comparison with the estimates for the normal slab-dip region, the observed Vs are ∼10–20% lower, thus yielding higher Vp/Vs (Fig. 7c). Previous models (e.g., Audet et al., 2009), however, have not considered underthrusting sediment (Calvert et al., 2011) and/or metasediment along the subduction channel (Breeding et al., 2004), which can also help explain observed seismic anomalies. Piana Agostinetti and Miller (2014) suggest that low velocity anomalies imaged with teleseismic converted phase may represent a mixture of underplated sediment, subducted crust, and/or serpentinized upper mantle. In addition to added pore fluid pressure, crack anisotropy might contribute to observed high Vp/Vs near the subduction zone plate interface (Wang et al., 2012).

6.3. Mantle hydration inducing the change in slab dip

Upon subduction, the fluids are released from the subducting slab in a series of metamorphic reactions, and the flux into the mantle wedge modifies its chemical and physical properties. The hydration of the mantle wedge decreases mantle rock strength significantly, and thus causes rheological weakening, melting and changes in the dynamics and thermal structure of the subduction zone systems. A low viscosity in the mantle wedge associated to the hydration has been argued to occur in Tonga–Kermadec subduction system (Billen and Gurnis, 2001). More recently, a presence of a low-viscosity channel atop the subducting crust is invoked by numerical calculations to support the current flat-slab configuration in central Mexico (Manea and Gurnis, 2007). The abundant occurrence of the mantle-derived minerals in the present-day subduction system probably would indicate that the mantle wedge had high H_2O concentration due to the dehydration of subducted sediments and oceanic crust, and that the mantle peridotite would react with slab fluids to form serpentinite (Kim et al., 2013). Kim et al. (2012b) further suggest that the central Mexican flat slab re-

gion is more hydrous than the region in south where the slab is dipping normal.

The subduction-related hydration plays a significant role in controlling shear wave velocities within the upper part of the oceanic crust and overlying mantle wedge, as evidenced in this study and previously from the case in central Mexico (Kim et al., 2013), and in central Chile (Porter et al., 2012). Similar to both subduction systems, we clearly observe differences in the compositions of the upper portion of the oceanic crust (LVZ; Figs. 5c, 6c, and 7b), and these may reflect different hydration degrees and furthermore the difference in slab geometry in southern Peru. As discussed in depth earlier, the flat portion of the slab appears more fluid-rich than the normal-dip region. The evidence of high H_2O content, bound in solid phases within the low-velocity layer, may explain the horizontal geometry of the Nazca Plate without strong coupling between subducting and overriding plates. The source of fluid may come from metasediments and subducted crust (Nazca Ridge), and these should influence overall subduction dynamics by contributing additional buoyancy of the slab and also lowering the viscosity of the overlying mantle wedge. We suggest that the continued supply of fluid due to the Nazca Ridge subduction supplies the missing ingredient to sustain the flat plate segment of about 800 km along the Peru Trench.

7. Conclusions

The subduction-related hydration plays a major role in controlling shear wave velocities within the upper part of the oceanic crust and overlying materials. We use data from the recent PeruSE seismic experiment in southern Peru to constrain degrees of hydration, and structural and mechanical properties of the oceanic crust between the normal-dip portion of the subduction interface and the flat slab–mantle interface. The analysis includes migration of teleseismic receiver functions and the inversion of the receiver function amplitudes to determine the variations in shear velocities within the subducted Nazca oceanic crust. The obtained values are compared to those determined from the experimental mineral physics data. We observe substantial shear velocity reductions of ~20–40% near the top plate interface in both regions. In particular, significant velocity reductions (additional ~20% reductions) and consequently higher P-to-S velocity ratio (exceeding 2.0) at the flat slab region suggest that the seismically probed subduction channel is fluid-rich and mechanically weak, which may explain lower interseismic coupling state. The major source of fluid comes from metasediments and Nazca Ridge. Continued supply of fluid from the southward migrating Nazca Ridge provides additional buoyancy of the subducting oceanic lithosphere. The change in mantle dynamics due to such long-term hydration would possibly lower the viscosity of the mantle wedge, facilitate slab flattening, and sustain the flat-slab configuration in southern Peru. Lastly, by separately examining the stations closest to the coast, we also suggest that the subduction of Nazca ridge can affect along-strike change in frictional behavior.

Acknowledgements

Appendix A. Supplementary material

Supplementary material related to this article can be found online at http://dx.doi.org/10.1016/j.epsl.2015.07.055.

References

Abers, G.A., 2005. Seismic low-velocity layer at the top of subducting slabs beneath volcanic arcs: observations, predictions, and systematics. Phys. Earth Planet. Inter. 149, 7–29. http://dx.doi.org/10.1016/j.pepi.2004.10.002.

ANCORP Working Group, 2003. Seismic imaging of a convergent continental margin and plateau in the central Andes (Andean Continental Research Project 1996 (ANCORP'96)). J. Geophys. Res. 108 (B7), 2328. http://dx.doi.org/10.1029/2002JB001771.

Audet, P., Bostock, M.G., Christensen, N.I., Peacock, S.M., 2009. Seismic evidence for overpressured subducted oceanic crust and megathrust fault sealing. Nature 457, 76–78. http://dx.doi.org/10.1038/nature07650.

Bezacier, L., Reynard, B., Bass, J.D., Sanchez-Valle, C., Van de Moortele, B., 2010. Elasticity of antigorite, seismic detection of serpentinites, and anisotropy in subduction zones. Earth Planet. Sci. Lett. 289, 198–208. http://dx.doi.org/10.1016/j.epsl.2009.11.009.

Bilek, S.L., 2010. Seismicity along the South American subduction zone: review of large earthquakes, tsunamis, and subduction zone complexity. Tectonophysics 495, 2–14. http://dx.doi.org/10.1016/j.tecto.2009.02.037.

Billen, M.I., Gurnis, M., 2001. A low viscosity wedge in subduction zones. Earth Planet. Sci. Lett. 193, 227–236.

Bostock, M.G., Hyndman, R.D., Rondenay, S.J., Peacock, S., 2002. An inverted continental Moho and the serpentinization of the forearc mantle. Nature 417, 536–538. http://dx.doi.org/10.1038/417536a.

Breeding, C.M., Ague, J.J., Brocker, M., 2004. Fluid-metasedimentary rock interactions in subduction-zone mélange: implications for the chemical composition of arc magmas. Geology 32, 1041–1044.

Cahill, T., Isacks, B.L., 1992. Seismicity and shape of the subducted Nazca Plate. J. Geophys. Res. 97 (B12), 17,503–17,529.

Calvert, A.J., Preston, L.A., Farahbod, A.M., 2011. Sedimentary underplating at the Cascadia mantle–wedge corner revealed by seismic imaging. Nat. Geosci. 4, 545–548. http://dx.doi.org/10.1038/NGEO1195.

Cande, S.C., 1985. Nazca–South American plate interaction since 50 my B.P. Present. In: Hussong, D.M., et al. (Eds.), Atlas of the Ocean Margin Program, Peru Continental Margin Region VI. Mar. Sci. Int., Woods Hole, Mass., p. 14.

Chlieh, M., Perfettini, H., Tavera, H., Avouac, J.-P., Remy, D., Nocquet, J.-M., Rolandone, F., Bondoux, F., Gabalda, G., Bonvalot, S., 2011. Interseismic coupling and seismic potential along the Central Andes subduction zone. J. Geophys. Res. 116, B12405. http://dx.doi.org/10.1029/2010JB008166.

Christensen, N.I., 1984. Pore pressure and oceanic crustal seismic structure. Geophys. J. R. Astron. Soc. 79, 411–423.

Clift, P.D., Pecher, I., Kukowski, N., Hampel, A., 2003. Tectonic erosion of the Peruvian Forearc, Lima Basin, by subduction and Nazca Ridge collision. Tectonics 22 (3). http://dx.doi.org/10.1029/2002TC001386.

Currie, C.A., Hyndman, R.D., 2006. The thermal structure of subduction zone back arcs. J. Geophys. Res. 111 (B08404). http://dx.doi.org/10.1029/2005JB004024.

DeMets, C., Gordon, G.R., Argus, D.F., 2010. Geologically current plate motions. Geophys. J. Int. 181, 1–80.

Ekström, G., Nettles, M., Dziewonski, A.M., 2012. The global CMT project 2004–2010: centroid-moment tensors for 13,017 earthquakes. Phys. Earth Planet. Inter. 200–201, 1–9. http://dx.doi.org/10.1016/j.pepi.2012.04.002.

Förste, C., et al., 2008. The GeoForschungsZentrum Potsdam/Groupe de Recherche de Géodésie Spatiale satellite-only and combined gravity field models: EIGEN-GL04S1 and EIGEN-GL04C. J. Geod. 82 (6), 331–346. http://dx.doi.org/10.1007/s00190-007-0183-8.

Gerya, T., Fossati, D., Cantieni, C., Seward, D., 2009. Dynamic effects of aseismic ridge subduction: numerical modeling. Eur. J. Mineral. 21, 649–661. http://dx.doi.org/10.1127/0935-1221/2009/0021-1931.

Gudmundsson, Ó., Sambridge, M., 1998. A regionalized upper mantle (RUM) seismic model. J. Geophys. Res. 103 (B4), 7121–7136. http://dx.doi.org/10.1029/97JB02488.

Gutscher, M.A., Spakman, W., Buwaard, H., Engdahl, E.R., 2000. Geodynamics of flat subduction: seismicity and tomographic constraints from the Andean margin. Tectonics 19 (5), 814–833. http://dx.doi.org/10.1029/1999TC001152.

Hacker, B.R., Abers, G.A., Peacock, S.M., 2003. Subduction factory 1. Theoretical mineralogy, densities, seismic wave speeds, and H_2O contents. J. Geophys. Res. 108, 2029. http://dx.doi.org/10.1029/2001JB001127.

Hampel, A., Kukowski, N., Bialas, J., Huebscher, C., Heinbockel, R., 2004. Ridge subduction at an erosive margin: the collision zone of the Nazca Ridge in southern Peru. J. Geophys. Res. 109, B02101. http://dx.doi.org/10.1029/2003JB002593.

Hansen, R.T.J., Bostock, M.G., Christensen, N.I., 2012. Nature of the low velocity zone in Cascadia from receiver function waveform inversion. Earth Planet. Sci. Lett. 337–338, 25–38. http://dx.doi.org/10.1016/j.epsl.2012.05.031.

Hayes, G.P., Wald, D.J., Johnson, R.L., 2012. Slab1.0: a three-dimensional model of global subduction zone geometries. J. Geophys. Res. 117, B01302. http://dx.doi.org/10.1029/2011JB008524.

Kim, Y., Clayton, R.W., Jackson, J.M., 2010. Geometry and seismic properties of the subducting Cocos plate in central Mexico. J. Geophys. Res. 115, B06310. http://dx.doi.org/10.1029/2009JB006942.

Kim, Y., Miller, M.S., Pearce, F., Clayton, R.W., 2012a. Seismic imaging of the Cocos plate subduction zone system in central Mexico. Geochem. Geophys. Geosyst. 13. http://dx.doi.org/10.1029/2012GC004033.

Kim, Y., Clayton, R.W., Jackson, J.M., 2012b. Distribution of hydrous minerals in the subduction system beneath Mexico. Earth Planet. Sci. Lett. 341–344, 58–67. http://dx.doi.org/10.1016/j.epsl.2012.06.001.

Kim, Y., Clayton, R.W., Asimow, P.D., Jackson, J.M., 2013. Generation of talc in the mantle wedge and its role in subduction dynamics in central Mexico. Earth Planet. Sci. Lett. 384, 81–87. http://dx.doi.org/10.1016/j.epsl.2013.10.006.

Kim, Y., Abers, G.A., Li, J., Christensen, D., Calkins, J., Rondenay, S., 2014. Alaska Megathrust 2: imaging the megathrust zone and Yakutat/Pacific plate interface in the Alaska subduction zone. J. Geophys. Res. 119, 1924–1941. http://dx.doi.org/10.1002/2013JB010581.

Krabbenhoft, A., Bialas, J., Kopp, H., Kukowski, N., Hubscher, C., 2004. Crustal structure of the Peruvian continental margin from wide-angle seismic studies. Geophys. J. Int. 159, 749–764. http://dx.doi.org/10.1111/j.1365-246X.2004.02425.x.

Laske, G., Masters, G., 1997. A global digital map of sediment thickness. EOS Trans. AGU 78, F483.

Ma, Y., R.W. Clayton, 2014. Structure of the flat slab in southern Peru. AGU T23A-4626 presented at 2014, Fall Meeting, AGU, San Francisco, CA, 15–19 December.

Manea, V.C., Gurnis, M., 2007. Subduction zone evolution and low viscosity wedges and channels. Earth Planet. Sci. Lett. 264, 22–45.

Mix, A.C., Tiedemann, R., Blum, P., et al., 2003. 8. Site 1237. In: Proceedings of the Ocean Drilling Program. Initial Reports, vol. 202.

Perfettini, H., et al., 2010. Seismic and aseismic slip on the central Peru megathrust. Nature 465, 78–81.

Phillips, K., et al., 2012. Structure of the subduction system in southern Peru from seismic array data. J. Geophys. Res. 117. http://dx.doi.org/10.1029/2012JB009540.

Phillips, K., Clayton, R.W., 2014. Structure of the subduction transition region from seismic array data in southern Peru. Geophys. J. Int. 196, 1889–1905. http://dx.doi.org/10.1093/gji/ggt504.

Piana Agostinetti, N., Miller, M.S., 2014. The fate of the downgoing oceanic plate: insight from the Northern Cascadia subduction zone. Earth Planet. Sci. Lett. 408, 237–251.

Pollack, H.N., Hurter, S.J., Johnson, J.R., 1993. Heat flow from the Earth's interior: analysis of the global data set. Rev. Geophys. 31 (3), 267–280. http://dx.doi.org/10.1029/93RG01249.

Porter, R., Gilbert, H., Zandt, G., Beck, S., Warren, L., Calkins, J., Alvarado, P., Anderson, M., 2012. Shear wave velocities in the Pampean flat-slab region from Rayleigh wave tomography: implications for slab and upper mantle hydration. J. Geophys. Res. 117, B11301. http://dx.doi.org/10.1029/2012JB009350.

Ramos, V.A., Folguera, A., 2009. Andean Flat-Slab Subduction Through Time. Special Publications, vol. 327. Geological Society, London, pp. 31–54.

Robinson, D.P., Das, S., Watts, A.B., 2006. Earthquake rupture stalled by a subducting fracture zone. Science 312, 1203–1205. http://dx.doi.org/10.1126/science.1125771.

Sandwell, D.T., Garcia, E., Soofi, K., Wessel, P., Smith, W.H.F., 2013. Towards 1 mGal global marine gravity from CryoSat-2, Envisat, and Jason-1. Lead. Edge 32 (8), 892–899. http://dx.doi.org/10.1190/tle32080892.1.

Skinner, S.M., Clayton, R.W., 2013. The lack of correlation between flat slabs and bathymetric impactors in South America. Earth Planet. Sci. Lett. 371–372, 1–5. http://dx.doi.org/10.1016/j.epsl.2013.04.013.

Swenson, J.L., Beck, S.L., 1996. Historical 1942 Ecuador and 1942 Peru subduction earthquakes, and earthquake cycles along Columbia Ecuador and Peru subduction segments. Pure Appl. Geophys. 146 (1), 67–101.

Syracuse, E.M., Abers, G.A., 2006. Global compilation of variations in slab depth beneath arc volcanoes and implications. Geochem. Geophys. Geosyst. 7, Q05017. http://dx.doi.org/10.1029/2005GC001045.

van Hunan, J., van den Berg, A.P., Vlaar, N.J., 2002. The impact of the South-American plate motion and the Nazca Ridge subduction on the flat subduction below South Peru. Geophys. Res. Lett. 29, 14. http://dx.doi.org/10.1029/2001GL014004. 1690.

Wang, K., Bilek, S.L., 2014. Fault creep caused by subduction of rough seafloor relief. Tectonophysics 610, 1–24. http://dx.doi.org/10.1016/j.tecto.2013.11.024.

Wang, X.-Q., Schubnel, A., Fortin, J., David, E.C., Gueguen, Y., Ge, H.-K., 2012. High Vp/Vs ratio: saturated cracks or anisotropy effects? Geophys. Res. Lett. 39, L11307. http://dx.doi.org/10.1029/2012GL051742.